Astrodynamics Vol. 7, No. 3, 285–299, 2023 https://doi.org/10.1007/s42064-023-0158-4

Optimal interplanetary trajectories for Sun-facing ideal diffractive sails

Alessandro A. Quarta, Giovanni Mengali, Marco Bassetto, and Lorenzo Niccolai (✉)

Department of Civil and Industrial Engineering, University of Pisa, I-56122 Pisa, Italy

ABSTRACT

A diffractive sail is a solar sail whose exposed surface is covered by an advanced diffractive metamaterial film with engineered optical properties. This study examines the optimal performance of a diffractive solar sail with a Sun-facing attitude in a typical orbit-to-orbit heliocentric transfer. A Sun-facing attitude, which can be passively maintained through the suitable design of the sail shape, is obtained when the sail nominal plane is perpendicular to the Sun–spacecraft line. Unlike an ideal reflective sail, a Sun-facing diffractive sail generates a large transverse thrust component that can be effectively exploited to change the orbital angular momentum. Using a recent thrust model, this study determines the optimal control law of a Sun-facing ideal diffractive sail and simulates the minimum transfer times for a set of interplanetary mission scenarios. It also quantifies the performance difference between Sun-facing diffractive sail and reflective sail. A case study presents the results of a potential mission to the asteroid 16 Psyche.

KEYWORDS

diffractive solar sail
Sun-facing sail
interplanetary transfer
trajectory optimization

Research Article

Received: 20 October 2022
Accepted: 17 January 2023

1 Introduction

The interaction between electromagnetic waves and matter is the working principle of photonic propulsion, a propellant-less technology that extracts momentum from solar radiation to generate thrust and navigate the solar system. An example of its effectiveness is provided by conventional solar sails [1, 2], which use a thin membrane to reflect the impinging photons coming from the Sun. The mechanism of photon reflection is exploited by other solar sail-based configurations such as heliogyros [3]. Following the success of the IKAROS demonstration mission [4–6], the reflective solar sail concept has become the focus of active research, as confirmed by the number of planned missions that will utilize this propulsion technology, including NASA's Near-Earth Asteroid Scout [7] and Solar Cruiser [8].

One of the main disadvantages of reflective solar sails is their limited capability to generate a transverse thrust component, in which the transverse means are perpendicular to the Sun–spacecraft line [9–11]. In particular, a Sun-facing reflective solar sail, characterized by a nominal plane normal to the Sun–spacecraft line, generates a purely radial propulsive acceleration; hence, it cannot modify the angular momentum of the osculating orbit. Other optical phenomena affecting the momentum transfer between incoming photons and the spacecraft have been investigated to deal with this problem.

For example, refraction or diffraction effects may be used to extract momentum from the solar radiation pressure and generate a suitable propulsive thrust [12]. In particular, a refractive sail can deflect incoming photons by refracting sunlight across a thin transparent membrane made of polymeric microprisms [13, 14], thereby producing a propulsive acceleration. Unlike a reflective solar sail, when microprisms are appropriately designed, a refractive sail can generate a large transverse thrust component even in a nearly Sun-facing orientation. This characteristic makes it easier to modify the specific angular momentum of the osculating orbit with a simple attitude control law. The unique capabilities of the refractive sail have attracted the interest of researchers. Firuzi and Gong [13] first addressed the problem of evaluating the radiation pressure applied to a refractive sail by a ray-tracing method [15] under the assumption that the refractive sail has no wrinkles or billowing effects and is perfectly transmissive. A recent study by Bassetto

✉ lorenzo.niccolai@unipi.it

Nomenclature

$\mathbb{A}$	state matrix with generic entry A_{ij}; see Eq. (9)
a	semi-major axis (au)
a_c	characteristic acceleration (m/s^2)
$\boldsymbol{a}_p$	propulsive acceleration vector (mm/s^2)
$\{a_{pR}, a_{pT}, a_{pN}\}$	components of $\boldsymbol{a}_p$ in $\mathcal{T}_{RTN}$
C	spacecraft center-of-mass
c	speed of light in vacuum (km/s)
D	dimensionless performance parameter; see Eq. (41)
$\boldsymbol{d}$	vector; see Eq. (9)
e	eccentricity
$\mathcal{H}$	Hamiltonian function
$I_\oplus$	solar irradiance at 1 au (W/m^2)
i	orbital inclination (deg)
$\{\hat{\boldsymbol{i}}_x, \hat{\boldsymbol{i}}_y, \hat{\boldsymbol{i}}_z\}$	unit vectors of $\mathcal{T}$
$\{\hat{\boldsymbol{i}}_R, \hat{\boldsymbol{i}}_T, \hat{\boldsymbol{i}}_N\}$	unit vectors of $\mathcal{T}_{RTN}$
J	performance index (day)
$\hat{\boldsymbol{K}}$	grating momentum unit vector
m	spacecraft total mass (kg)
$\{p, f, g, h, k, L\}$	modified equinoctial orbital elements
$\mathcal{T}(C; x, y, z)$	body reference frame
$\mathcal{T}_{RTN}(C; R, T, N)$	radial–tangential–normal reference frame
r	Sun–spacecraft distance (au)
$r_\oplus$	reference distance (1 au)
t	time (day)
$\boldsymbol{x}$	spacecraft state vector
δ	clock angle (deg)
$\boldsymbol{\lambda}$	costate vector
ν	spacecraft true anomaly (deg)
Ω	right ascension of the ascending node (deg)
ω	argument of perihelion (deg)

Subscripts

0	initial value
i	parking orbit
f	final value, target orbit
IRS	related to IRS
SFIDS	related to SFIDS

Superscripts

$\cdot$	time derivative
$\star$	optimal value
$'$	depending on the control δ

et al. [16] proposed a semi-analytical thrust vector model to analyze a set of minimum-time circle-to-circle orbit transfers of a refractive sail-based spacecraft.

A typical refractive sail is designed to minimize the light diffraction through the microprism film. This requires the shortest side of the microprisms to be at least ten times greater than the longest wavelength [17]. The diffraction of sunlight can also be exploited to generate thrust. More precisely, the working principle of a diffractive sail involves the use of a metamaterial film to diffract incoming photons, which are deflected from their original path to generate a net propulsive acceleration. In a typical configuration, the diffractive film consists of a polarization grating with a period comparable to the wavelength of the incoming electromagnetic radiation. In principle, many other complex metamaterials may be used with potential advantages in sail performance and thrust-vectoring capability [18].

Recent studies have demonstrated the interest of the scientific community in this innovative propulsive concept. The study by Swartzlander [18] compared the performance of Sun-facing diffractive sails, Littrow diffraction configurations, and conventional reflective sails in the context of Earth–Mars transfers without using an optimal approach. In particular, under the assumption of a constant sail attitude with respect to the Sun–spacecraft line, a transparent diffractive sail was found to be superior to a reflective sail because the latter requires more time to reach the target orbit [18]. Another study by Swartzlander [19] showed that a diffraction film with a grating period of 1 μm can convert 83% of the solar blackbody spectrum into spacecraft momentum. Moreover, the non-optimized orbit-raising trajectories of diffractive and reflective sails were compared, and the potential advantages of the former were described. Srivastava and Swartzlander [20] described the optomechanics of a rigid nonspinning light sail that mitigated a catastrophic sail walk-off and tumbling using a flat axicon diffraction grating. Other recent studies by Serak *et al.* [21], Srivastava *et al.* [22], Chu *et al.* [23], and Chu *et al.* [24] confirmed the potential of this technology in the field of solar sail research.

An interesting feature of the diffractive sail is its ability to provide a large transverse component of thrust, even when its nominal plane is orthogonal to the Sun–spacecraft line. This intrinsic characteristic was described in detail by Dubill and Swartzlander [25], which is taken as the starting point of this paper. In particular, Dubill and Swartzlander [25] attempted to maneuver an interplanetary diffractive sail-based light spacecraft to

increase the orbital inclination while reducing its distance from the Sun from 1 to 0.32 au with a flight time of approximately 6 years. Such a mission scenario could allow a constellation of diffractive solar sails (or smart dust [26–28]) to be placed around the Sun to collect images and other data for space weather monitoring and heliophysics science. The interest in such missions has been confirmed by the research program on solar photonic propulsion recently promoted by the Italian Space Agency [29, 30].

Based on the results of Ref. [25], the aim of this study is to develop an analytical expression of the time-optimal steering law [31, 32] for a Sun-facing ideal diffractive sail (SFIDS). The thrust control variable was represented by the clock angle, which provides the angular position of the sail body-fixed reference frame with respect to the radial direction. An in-orbit variation of the clock angle may be obtained using a reaction wheel [25] capable of generating a torque along the spacecraft body axis aligned with the Sun–spacecraft line. The optimal steering law was then used to analyze typical heliocentric transfer trajectories in the preliminary mission design phase, including a transfer toward an asteroid [33–35].

The remainder of this paper is organized as follows. Section 2 describes the diffractive sail propulsive acceleration model, starting from the literature. Section 3 analyzes the optimal steering law, which is specialized in Section 4 for a set of minimum-time interplanetary transfers. Section 5 deals with the optimal transfers toward the asteroid 16 Psyche, while Section 6 presents some concluding remarks.

2 Orbital dynamics and sail thrust model description

Consider a spacecraft equipped with a diffractive solar sail as its primary propulsion system. The spacecraft initially covers a heliocentric parking orbit (subscript i) defined by a given set of modified equinoctial orbital elements (MEOEs) $\{p_i, f_i, g_i, h_i, k_i\}$ [36, 37]. Recall that the classical orbital elements $\{a, e, i, \Omega, \omega\}$ can be calculated from the five MEOEs $\{p, f, g, h, k\}$ using Eqs. (1)–(5):

$$a = \frac{p}{1 - f^2 - g^2} \tag{1}$$

$$e = \sqrt{f^2 + g^2} \tag{2}$$

$$i = 2\arctan\sqrt{h^2 + k^2} \tag{3}$$

$$\sin\omega = gh - fk, \quad \cos\omega = fh + gk \tag{4}$$

$$\sin\Omega = k, \quad \cos\Omega = h \tag{5}$$

where a is the semi-major axis, e is the eccentricity, i is the orbital inclination with respect to the ecliptic at epoch J2000.0, Ω is the longitude of the ascending node, and ω is the argument of perihelion. According to Eqs. (1) and (2), the MEOE p coincides with the semilatus rectum of the spacecraft's osculating orbit. The spacecraft true anomaly ν can be expressed as a function of the true longitude L (the last of the six MEOEs [36, 37]) by

$$\nu = L - \Omega - \omega \tag{6}$$

Following Betts [38], spacecraft heliocentric dynamics can be described by introducing the state vector $\boldsymbol{x} \in \mathbb{R}^{6\times1}$ defined as

$$\boldsymbol{x} \triangleq [p, f, g, h, k, L]^{\mathrm{T}} \tag{7}$$

whose time derivative is expressed as a function of the spacecraft propulsive acceleration vector $\boldsymbol{a}_{\mathrm{p}} \in \mathbb{R}^{3\times1}$ as

$$\dot{\boldsymbol{x}} = \mathbb{A}\,\boldsymbol{a}_{\mathrm{p}} + \boldsymbol{d} \tag{8}$$

where $\mathbb{A} \in \mathbb{R}^{6\times3}$ and $\boldsymbol{d} \in \mathbb{R}^{6\times1}$ are given by

$$\mathbb{A} \triangleq \begin{bmatrix} 0 & A_{12} & 0 \\ A_{21} & A_{22} & A_{23} \\ A_{31} & A_{32} & A_{33} \\ 0 & 0 & A_{43} \\ 0 & 0 & A_{53} \\ 0 & 0 & A_{63} \end{bmatrix}, \quad \boldsymbol{d} \triangleq \begin{bmatrix} 0 \\ 0 \\ 0 \\ 0 \\ 0 \\ d_6 \end{bmatrix} \tag{9}$$

with

$$A_{12} = \frac{2p}{1 + f\cos L + g\sin L}\sqrt{\frac{p}{\mu_\odot}} \tag{10}$$

$$A_{21} = \sin L\sqrt{\frac{p}{\mu_\odot}} \tag{11}$$

$$A_{22} = \frac{(2 + f\cos L + g\sin L)\cos L + f}{1 + f\cos L + g\sin L}\sqrt{\frac{p}{\mu_\odot}} \tag{12}$$

$$A_{23} = -\frac{g\,(h\sin L - k\cos L)}{1 + f\cos L + g\sin L}\sqrt{\frac{p}{\mu_\odot}} \tag{13}$$

$$A_{31} = -\cos L\sqrt{\frac{p}{\mu_\odot}} \tag{14}$$

$$A_{32} = \frac{(2 + f\cos L + g\sin L)\sin L + g}{1 + f\cos L + g\sin L}\sqrt{\frac{p}{\mu_\odot}} \tag{15}$$

$$A_{33} = \frac{f\,(h\sin L - k\cos L)}{1 + f\cos L + g\sin L}\sqrt{\frac{p}{\mu_\odot}} \tag{16}$$

$$A_{43} = \frac{\left(1 + h^2 + k^2\right)\cos L}{2\,(1 + f\cos L + g\sin L)}\sqrt{\frac{p}{\mu_\odot}} \tag{17}$$

$$A_{53} = \frac{\left(1 + h^2 + k^2\right)\sin L}{2\,(1 + f\cos L + g\sin L)}\sqrt{\frac{p}{\mu_\odot}} \tag{18}$$

$$A_{63} = \frac{h\sin L - k\cos L}{1 + f\cos L + g\sin L}\sqrt{\frac{p}{\mu_\odot}} \tag{19}$$

$$d_6 = \sqrt{\mu_\odot p}\left(\frac{1+f\cos L+g\sin L}{p}\right)^2 \tag{20}$$

where $\mu_\odot$ is the Sun's gravitational parameter. The vectorial differential equation (8) is completed using the initial conditions in Eq. (21) defined at the initial time $t = t_0 \triangleq 0$:

$$\boldsymbol{x}(t_0) = \boldsymbol{x}_0 \triangleq [p_i, f_i, g_i, h_i, k_i, L_0]^{\mathrm{T}} \tag{21}$$

where $L_0 \triangleq L(t_0)$ is the true longitude at time t_0, which can be calculated by Eq. (6) as a function of the initial spacecraft true anomaly $\nu_0 \triangleq \nu(t_0)$ on the heliocentric parking orbit.

In Eq. (8), the three components $\{a_{\mathrm{p}R}, a_{\mathrm{p}T}, a_{\mathrm{p}N}\}$ of the spacecraft propulsive acceleration vector $\boldsymbol{a}_{\mathrm{p}}$ are expressed in a radial–tangential–normal reference frame $\mathcal{T}_{\mathrm{RTN}}(C; R, T, N)$ of the unit vectors $\{\hat{\boldsymbol{i}}_R, \hat{\boldsymbol{i}}_T, \hat{\boldsymbol{i}}_N\}$. The origin of $\mathcal{T}_{\mathrm{RTN}}$ coincides with the spacecraft center-of-mass C. The R-axis lies along the Sun–spacecraft line (i.e., along the direction of the unit vector $\hat{\boldsymbol{i}}_R$). The T-axis belongs to the osculating orbit plane and points toward the direction of the spacecraft (inertial) velocity vector. The N-axis coincides with the direction of the spacecraft angular momentum vector, as shown in Fig. 1.

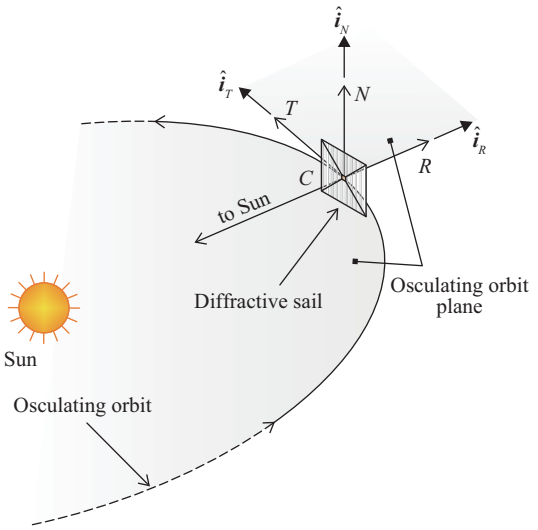

Fig. 1 Orbital reference frame $\mathcal{T}_{\mathrm{RTN}}$.

The propulsive acceleration vector (and its components) can be described as a function of the spacecraft attitude using a suitable diffractive sail thrust model. A mathematical model was first proposed by Swartzlander [18]. This propulsion system representation, which can be considered as the counterpart of the well-known ideal reflective sail (IRS) force model [9, 39] for a diffractive sail, was recently adapted by Dubill and Swartzlander [25] to the special case of a Sun-facing sail [40, 41]. Note that this particular attitude can be passively maintained by choosing a suitable sail shape [42], that is, by designing a slightly conical surface with the apex directed toward the Sun [43].

Based on the analytical results obtained in Refs. [18, 25], the thrust model of an SFIDS can be described by introducing a right-handed body-fixed reference frame $\mathcal{T}(C; x, y, z)$ of origin C and unit vectors $\{\hat{\boldsymbol{i}}_x, \hat{\boldsymbol{i}}_y, \hat{\boldsymbol{i}}_z\}$, as shown in Fig. 2. The (x, y) plane coincides with the sail nominal plane, while the x-axis is in the opposite direction of the grating momentum unit vector $\hat{\boldsymbol{K}}$, that is, $\hat{\boldsymbol{i}}_x = -\hat{\boldsymbol{K}}$. Recall that the grating vector of the sail film structure is aligned with the direction of periodicity of the grating [44].

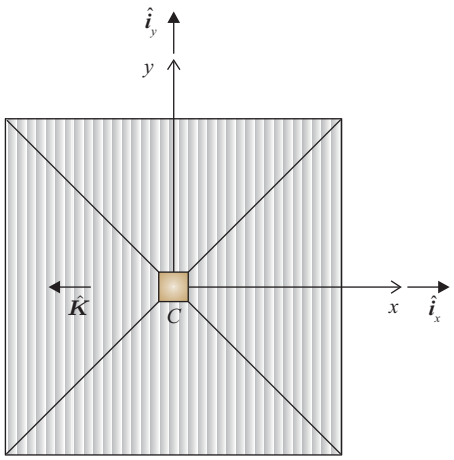

Fig. 2 Diffractive sail body reference frame $\mathcal{T}(C; x, y, z)$ and grating momentum unit vector $\hat{\boldsymbol{K}}$.

According to Dubill and Swartzlander [25], when the z-axis of the body reference frame is aligned with the Sun–spacecraft line, that is, in a Sun-facing condition with $z \equiv R$ and $\hat{\boldsymbol{i}}_R \equiv \hat{\boldsymbol{i}}_z$, the propulsive acceleration vector $\boldsymbol{a}_{\mathrm{p}}$ can be written as

$$\boldsymbol{a}_{\mathrm{p}} = \frac{I_\oplus S}{mc}\left(\frac{r_\oplus}{r}\right)^2\left(\hat{\boldsymbol{i}}_z + \hat{\boldsymbol{i}}_x\right) \tag{22}$$

where r is the Sun–spacecraft distance, S is the area of the sail reflective surface, c is the speed of light in vacuum, m is the total mass of the spacecraft (assumed to be constant), and $I_\oplus$ is the solar irradiance at a distance $r = r_\oplus \triangleq 1$ au from the Sun. According to Eq. (22), in a Sun-facing condition, the sail propulsive acceleration vector belongs to the plane (x, z) of the body reference frame $\mathcal{T}$, and $\boldsymbol{a}_{\mathrm{p}}$ forms 45 deg angle with the Sun–spacecraft

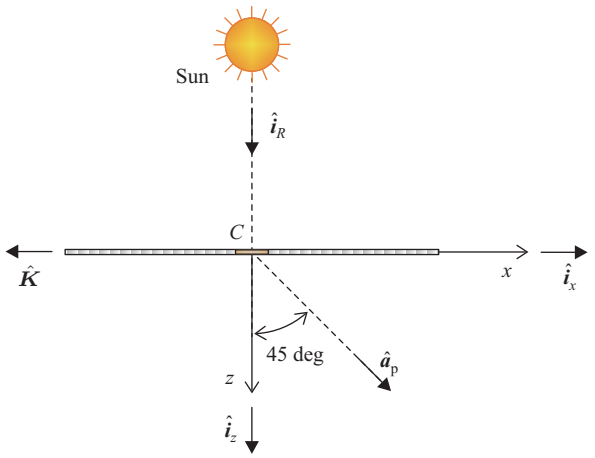

Fig. 3 SFIDS propulsive acceleration vector direction in the body reference frame $\mathcal{T}(C; x, y, z)$.

line, as shown in Fig. 3, where $\hat{\boldsymbol{a}}_\mathrm{p} \triangleq \boldsymbol{a}_\mathrm{p}/\|\boldsymbol{a}_\mathrm{p}\|$ is the propulsive acceleration unit vector. Equation (22) can be rewritten in a more compact form by introducing the characteristic acceleration a_c [9]: Analogous to the IRS case, a_c is defined as the maximum value of the propulsive acceleration magnitude $\|\boldsymbol{a}_\mathrm{p}\|$ when $r = r_\oplus$. Taking Eq. (22) into account, a_c is expressed as

$$a_\mathrm{c} = \frac{\sqrt{2} I_\oplus S}{mc} \tag{23}$$

Such that the propulsive acceleration vector can be rewritten as

$$\boldsymbol{a}_\mathrm{p} = \frac{a_\mathrm{c}}{\sqrt{2}} \left(\frac{r_\oplus}{r}\right)^2 \left(\hat{\boldsymbol{i}}_z + \hat{\boldsymbol{i}}_x\right) \tag{24}$$

The three components $\{a_{\mathrm{p}R}, a_{\mathrm{p}T}, a_{\mathrm{p}N}\}$ of the propulsive acceleration required to complete the vectorial differential equation (8) were obtained by projecting $\boldsymbol{a}_\mathrm{p}$ onto the radial–tangential–normal reference frame $\mathcal{T}_\mathrm{RTN}$. To this end, we introduce the sail clock angle $\delta \in [-180, 180)$ deg, defined as the angle, measured counterclockwise, between the T-axis and x-axis, as shown in Fig. 4, where $\hat{\boldsymbol{n}}$ is the unit vector normal to the sail nominal plane in the direction opposite the Sun (i.e., the shadowed side of the sail). From Fig. 4 we obtain

$$\hat{\boldsymbol{i}}_x = \hat{\boldsymbol{i}}_T \cos\delta + \hat{\boldsymbol{i}}_N \sin\delta \tag{25}$$

and recalling that $\hat{\boldsymbol{i}}_z \equiv \hat{\boldsymbol{i}}_R$ in a Sun-facing condition, Eqs. (24) and (25) yield

$$\boldsymbol{a}_\mathrm{p} = \frac{a_\mathrm{c}}{\sqrt{2}} \left(\frac{r_\oplus}{r}\right)^2 \left(\hat{\boldsymbol{i}}_R + \hat{\boldsymbol{i}}_T \cos\delta + \hat{\boldsymbol{i}}_N \sin\delta\right) \tag{26}$$

such that the components $\{a_{\mathrm{p}R}, a_{\mathrm{p}T}, a_{\mathrm{p}N}\}$ are reduced to

$$a_{\mathrm{p}R} = \frac{a_\mathrm{c}}{\sqrt{2}} \left(\frac{r_\oplus}{r}\right)^2 \tag{27}$$

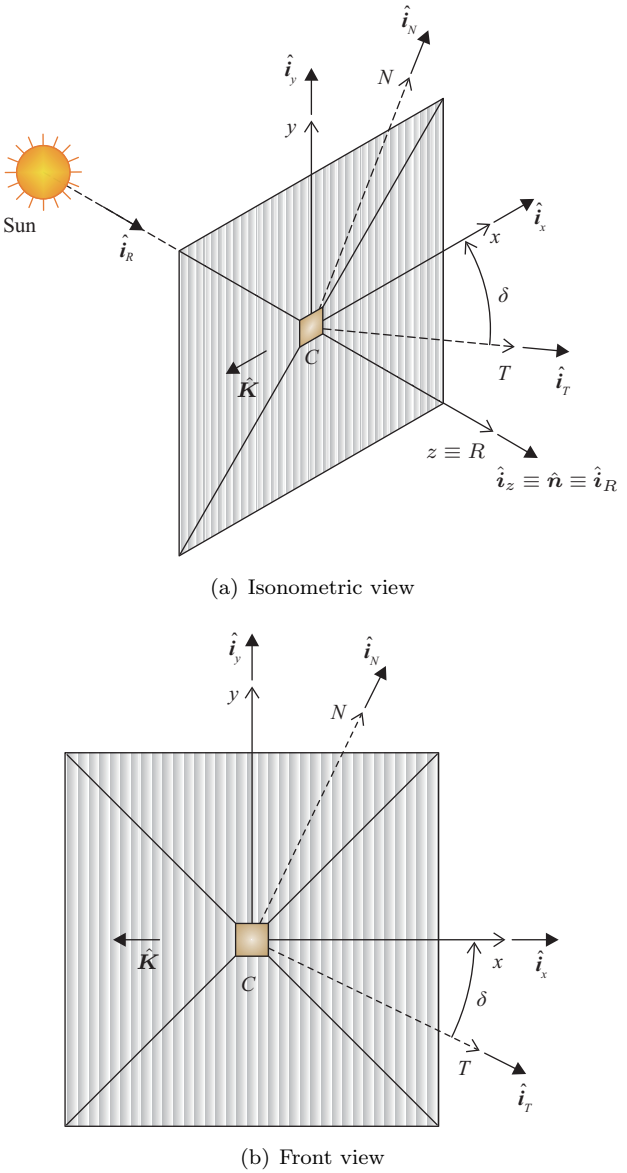

(a) Isonometric view

(b) Front view

Fig. 4 Sail clock angle δ in a Sun-facing condition.

$$a_{\mathrm{p}T} = \frac{a_\mathrm{c}}{\sqrt{2}} \left(\frac{r_\oplus}{r}\right)^2 \cos\delta \tag{28}$$

$$a_{\mathrm{p}N} = \frac{a_\mathrm{c}}{\sqrt{2}} \left(\frac{r_\oplus}{r}\right)^2 \sin\delta \tag{29}$$

According to Eq. (26), for a given value of a_c and distance r from the Sun, the SFIDS thrust vector is dependent only on the value of the clock angle δ, which therefore represents the single control variable.

Note that an IRS (when not constrained to maintain a Sun-facing attitude) has two control variables: the clock and cone angle. The latter is defined as the angle between $\hat{\boldsymbol{n}}$ and the Sun–spacecraft line. The form of the SFIDS propulsive acceleration vector given by Eq. (26) is very

different from the general expression used for an IRS without optical degradation [45] and wrinkles [46, 47]. Such a difference can be observed in Fig. 5, which shows a typical sail force bubble (i.e., the locus of the propulsive acceleration vector arrow) for an SFIDS and an IRS of equal characteristic acceleration.

Figure 5 shows that the SFIDS thrust vector belongs to a conical surface coaxial in the radial (i.e., Sun–spacecraft) direction with a half angle of 45 deg, as shown in Fig. 6. In particular, Fig. 5 highlights that an SFIDS provides a single value for the transverse component of the propulsive acceleration vector that is significantly greater than the maximum transverse value achieved with an IRS of equal characteristic acceleration. Figure 5 also shows that in a "diffractive case", $\|\boldsymbol{a}_{\mathrm{p}}\| \neq 0$, that is, a coasting arc cannot be generated in the SFIDS trajectory design. Coasting arcs are often required in the time-optimal transfer trajectory of a solar sail-based spacecraft [48, 49]. This raises the question of the performance difference between a common IRS and an SFIDS in a heliocentric minimum-time transfer scenario, which will be discussed in Section 4. Section 3 presents the analysis of the optimal control law and optimal trajectory characteristics of an SFIDS-based mission.

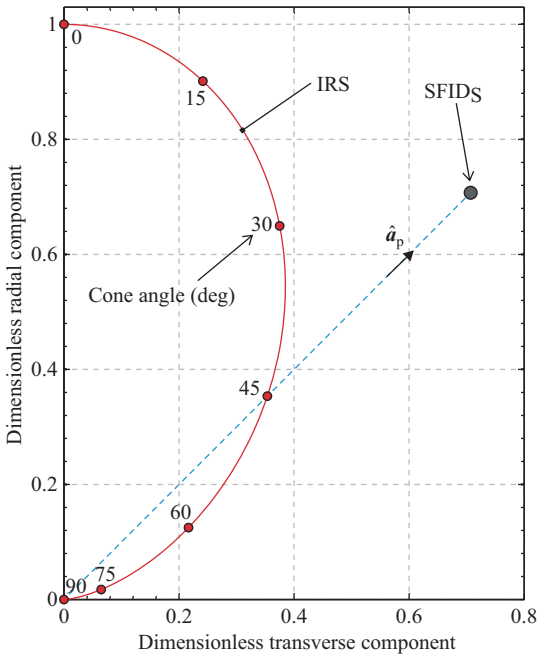

Fig. 5 Force bubble for an ideal reflective sail and an ideal Sun-facing diffractive sail.

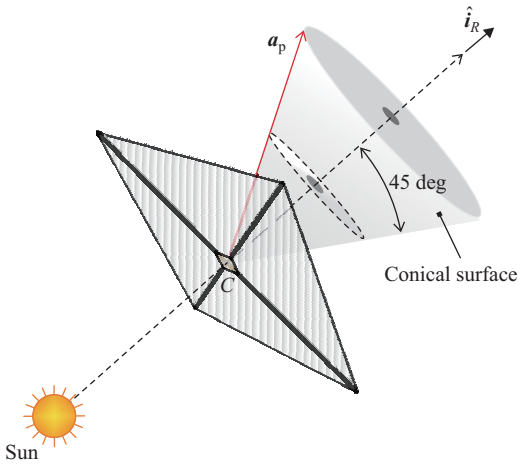

Fig. 6 SFIDS propulsive acceleration vector.

3 Trajectory optimization

The performance of SFIDS and IRS in a three-dimensional heliocentric mission case is compared. To that end, consider an optimal orbit-to-orbit interplanetary transfer, in which the sail thrust vector is steered in such a way to minimize the flight time required to transfer the spacecraft from the Earth's heliocentric orbit to that of the target celestial body. In an orbit-to-orbit transfer, the spacecraft angular position remains free at both the beginning and end of the transfer phase to obtain the minimum value of the performance index (i.e., flight time) within the context of an ephemeris-free mission scenario. Accordingly, the values of the spacecraft's true anomalies along the parking and target heliocentric orbits are the outputs of the optimization process. The mathematical model that provides the optimal transfer trajectories of an IRS-based spacecraft was discussed in Ref. [50]. The case of an SFIDS is analyzed in this section.

The heliocentric orbit of a given celestial body is defined by the set $\{p, f, g, h, k\}$ of MEOEs. Using the SFIDS thrust model discussed in Section 2, the optimization problem requires the determination of the time variation of the sail clock angle δ that maximizes the performance index:

$$J \triangleq -(t_{\mathrm{f}} - t_0) \equiv -t_{\mathrm{f}} \tag{30}$$

with boundary constraints:

$$\begin{aligned} &p(t_0) = p_{\mathrm{i}},\ f(t_0) = f_{\mathrm{i}},\ g(t_0) = g_{\mathrm{i}},\\ &h(t_0) = h_{\mathrm{i}},\ k(t_0) = k_{\mathrm{i}} \end{aligned} \tag{31}$$

$$\begin{aligned} &p(t_{\mathrm{f}}) = p_{\mathrm{f}},\ f(t_{\mathrm{f}}) = f_{\mathrm{f}},\ g(t_{\mathrm{f}}) = g_{\mathrm{f}},\\ &h(t_{\mathrm{f}}) = h_{\mathrm{f}},\ k(t_{\mathrm{f}}) = k_{\mathrm{f}} \end{aligned} \tag{32}$$

where the set $\{p_\mathrm{f}, f_\mathrm{f}, g_\mathrm{f}, h_\mathrm{f}, k_\mathrm{f}\}$ denotes the characteristics of the heliocentric target orbit.

The optimization problem was solved with an indirect approach [51, 52]. Recalling Eq. (8), the Hamiltonian function is written as

$$\mathcal{H} \triangleq \boldsymbol{\lambda} \cdot (\mathbb{A}\boldsymbol{a}_\mathrm{p}) + \boldsymbol{\lambda} \cdot \boldsymbol{d} \tag{33}$$

where $\boldsymbol{\lambda} \in \mathbb{R}^{6\times 1}$ is the costate vector defined as

$$\boldsymbol{\lambda} \triangleq [\lambda_p, \lambda_f, \lambda_g, \lambda_h, \lambda_k, \lambda_L]^\mathrm{T} \tag{34}$$

and $\{\lambda_p, \lambda_f, \lambda_g, \lambda_h, \lambda_k, \lambda_L\}$ are six costates. The time derivatives of the costates are given by the Euler–Lagrange equations:

$$\dot{\boldsymbol{\lambda}} = -\frac{\partial \mathcal{H}}{\partial \boldsymbol{x}} \tag{35}$$

where $\boldsymbol{x}$ denotes the state vector defined in Eq. (7). The Euler–Lagrange equations were derived from Eq. (35) in analytical form using Eqs. (9)–(20). However, their explicit expressions are omitted here for brevity.

The optimal time variation of the clock angle $\delta = \delta^\star(t)$ was obtained by applying Pontryagin's maximum principle, that is, by maximizing at any time instant the portion $\mathcal{H}'$ of the Hamiltonian function $\mathcal{H}$ that is explicitly dependent on the control angle δ, or

$$\mathcal{H}' \triangleq \boldsymbol{\lambda} \cdot (\mathbb{A}\,\boldsymbol{a}_\mathrm{p}) \tag{36}$$

Using Eqs. (9)–(19) and (27)–(29), the necessary condition $\partial\mathcal{H}'/\partial\delta = 0$ provides the expression of the optimal clock angle as a function of the spacecraft states and costates.

$$\sin\delta^\star = -\frac{A_{63}\lambda_L + A_{23}\lambda_f + A_{33}\lambda_g + A_{43}\lambda_h + A_{53}\lambda_k}{\sqrt{\begin{array}{c}(A_{63}\lambda_L + A_{23}\lambda_f + A_{33}\lambda_g + A_{43}\lambda_h + A_{53}\lambda_k)^2 \\ + (A_{22}\lambda_f + A_{32}\lambda_g + A_{12}\lambda_p)^2\end{array}}} \tag{37}$$

$$\cos\delta^\star = -\frac{A_{22}\lambda_f + A_{32}\lambda_g + A_{12}\lambda_p}{\sqrt{\begin{array}{c}(A_{63}\lambda_L + A_{23}\lambda_f + A_{33}\lambda_g + A_{43}\lambda_h + A_{53}\lambda_k)^2 \\ + (A_{22}\lambda_f + A_{32}\lambda_g + A_{12}\lambda_p)^2\end{array}}} \tag{38}$$

The solution of the optimization problem requires the numerical integration of a set of 12 nonlinear scalar differential equations provided by Eqs. (8) and (35). Ten of the twelve necessary boundary conditions are given by Eqs. (31) and (32). The last two boundary conditions were obtained by enforcing the transversality condition [53].

$$\lambda_L(t_0) = 0, \quad \lambda_L(t_\mathrm{f}) = 0 \tag{39}$$

Bearing in mind Eq. (30), the transversality condition [53] also applies an additional constraint on the final value of the Hamiltonian function, which is useful for calculating the unknown flight time t_f.

$$\mathcal{H}(t_\mathrm{f}) = 1 \tag{40}$$

The associated two-point boundary value problem (TPBVP) was solved with an absolute error of less than 10^{-8} through a hybrid numerical technique that uses gradient-based methods to obtain the optimal flight time and unknown initial value of the costates $\{\lambda_p, \lambda_f, \lambda_g, \lambda_h, \lambda_k\}$. It should be noted that the initial value of λ_L was obtained from Eq. (40). During the solution of the associated TPBVP, the spacecraft equations of motion and the Euler–Lagrange equations were numerically integrated using a variable order Adams–Bashforth–Moulton solver scheme [54] with absolute and relative errors of 10^{-10}.

For a given value of the sail performance parameter a_c and a given target celestial body, the previously described optimization problem was solved to obtain the minimum flight time t_f. Therefore, it is possible to graphically determine the function $t_\mathrm{f} = t_\mathrm{f}(a_\mathrm{c})$ by simply repeating the same procedure for different values of a_c. This aspect will be analyzed in Section 4 for a set of potential interplanetary mission scenarios, along with a numerical performance comparison with an IRS-based spacecraft.

4 Numerical results and SFIDS–IRS comparison

The procedure described in Section 3 was used to evaluate the optimal transfer performance of an SFIDS-based spacecraft in an interplanetary mission to Mercury, Venus, and Mars. The orbital elements of the celestial bodies involved in the numerical simulations were obtained through the JPL Horizons online ephemeris system (all the data were from July 1, 2022). The orbital characteristics, in terms of classical orbital elements and MEOEs, are summarized in Table 1. The table also includes the data of the asteroid 16 Psyche, which will be considered as a case study in Section 5.

In each three-dimensional mission case (Earth–Mercury, Earth–Venus, and Earth–Mars), parametric analysis was performed to evaluate the sensitivity of the minimum flight time t_f to the value of the characteristic acceleration, which was assumed to vary within the range

Table 1 Classical orbital elements and MEOEs used in the numerical simulations. Data refer to the actual planetary ephemeris on July 1, 2022, according to the JPL Horizons system

	Earth	Mercury	Venus	Mars	16 Psyche
a (au)	1.0008	3.8710×10^{-1}	7.2333×10^{-1}	1.5238	2.9244
e	1.5940×10^{-2}	2.0563×10^{-1}	6.7483×10^{-3}	9.3502×10^{-2}	1.3402×10^{-1}
i (deg)	3.0226×10^{-3}	7.0036	3.3944	1.8479	3.0969
Ω (deg)	1.5986×10^{2}	4.8302×10^{1}	7.6617×10^{1}	4.9490×10^{1}	1.5003×10^{2}
ω (deg)	3.0298×10^{2}	2.9188×10^{1}	5.4719×10^{1}	2.8672×10^{2}	2.2925×10^{2}
p (au)	1.0005	3.7073×10^{-1}	7.2330×10^{-1}	1.5105	2.8719
f	-3.5430×10^{-3}	4.4540×10^{-2}	-4.4571×10^{-3}	8.5555×10^{-2}	1.2650×10^{-1}
g	1.5542×10^{-2}	2.0074×10^{-1}	5.0669×10^{-3}	-3.7722×10^{-2}	4.4256×10^{-2}
h	-2.4765×10^{-5}	4.0707×10^{-2}	6.8580×10^{-3}	1.0476×10^{-2}	-2.3419×10^{-2}
k	9.0802×10^{-6}	4.5692×10^{-2}	2.8826×10^{-2}	1.2262×10^{-2}	1.3503×10^{-2}

$a_c \in [0.1, 1]$ mm/s^2. For reflective solar sails, a_c values of approximately 0.1 mm/s^2 indicate a low-performance sail. A propulsion system with a characteristic acceleration of approximately 1 mm/s^2 can be considered as a medium-high performance sail. In particular, a value of $a_c \approx 0.1$ mm/s^2 represents the state-of-the-art of the (reflective) sail technology. For example, the design value of the characteristic acceleration of the upcoming NASA mission Solar Cruiser [8] is approximately 0.12 mm/s^2, while the recently proposed mission concept of Helianthus [30, 55] has a design value of approximately 0.6 mm/s^2.

The numerical results in terms of the minimum flight time t_f as a function of a_c for an SFIDS-based spacecraft are summarized in Fig. 7 for the three interplanetary mission cases. The difference in flight times between SFIDS- and IRS-based spacecraft was quantified with the dimensionless parameter:

$$D \triangleq \frac{t_f|_{\text{IRS}} - t_f|_{\text{SFIDS}}}{t_f|_{\text{SFIDS}}} \tag{41}$$

where $t_f|_{\text{SFIDS}}$ (or $t_f|_{\text{IRS}}$) is the minimum flight time obtained by solving an optimal control problem for an SFIDS-based (or IRS-based) spacecraft. For a given a_c, a positive value of D indicates that the performance of the SFIDS is superior to that of the IRS, that is, the SFIDS enables the spacecraft to reach the target planet in a shorter flight time compared with the IRS case. The function $D = D(a_c)$, obtained numerically, is plotted in Fig. 8. Note that this comparison assumes that the SFIDS and IRS have the same characteristic acceleration a_c; however, in principle, the SFIDS should have a smaller area-to-mass ratio than the IRS. A more detailed estimate of the achievable level of performance with an SFIDS is beyond the scope of this study.

Figure 8 shows that in each mission scenario, the SFIDS performance is superior to that of the IRS for the entire range of characteristic accelerations considered in the numerical simulations. The percentage difference in flight times was more pronounced when smaller values of the characteristic acceleration were considered. For example, in a three-dimensional Earth–Mars orbit-to-orbit transfer with a medium-high performance sail, the flight time in the IRS-based case was approximately 15%–20% greater than that required by the SFIDS. The percentage difference increased to approximately 70%–90% for a low-performance sail. The ripples in Fig. 8 were attributed to the slight variations in the flight time when the spacecraft swept angle is an integer multiple of 2π, as discussed in Refs. [3, 56] with a simplified (two-dimensional) mission scenario involving a reflective sail.

The curves in Figs. 7 and 8 show that the difference in the transverse component of the propulsive acceleration vector between the SFIDS and IRS (highlighted in Fig. 5) has a major effect on the transfer performance, despite the higher maneuverability characteristics of the IRS. Recall that the IRS has two control variables (i.e., two control angles), while the thrust vector of the SFIDS is dependent only on the clock angle. The characteristics of the optimal transfer trajectory of the SFIDS-based spacecraft are analyzed in Section 5 in a more challenging orbit-to-orbit mission scenario.

5 Case study

In this section, we consider a mission to the asteroid 16 Psyche, a small body located in the belt between Mars and Jupiter. The asteroid is a potential target of exploration in the near future [57] because of its particular metal-rich composition [58–60]. In fact NASA and the Jet Propulsion Laboratory planned a robotic

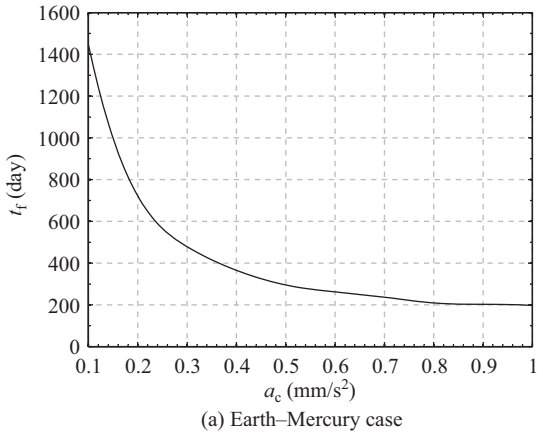

(a) Earth–Mercury case

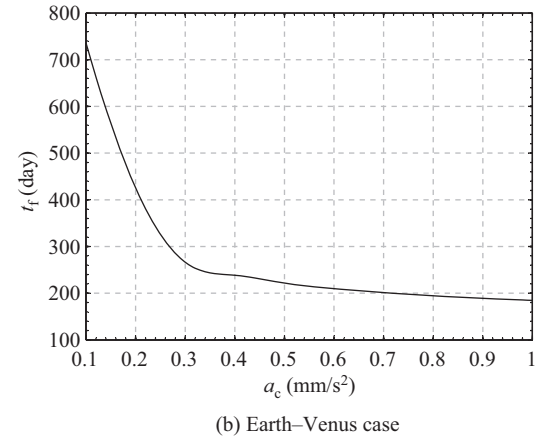

(b) Earth–Venus case

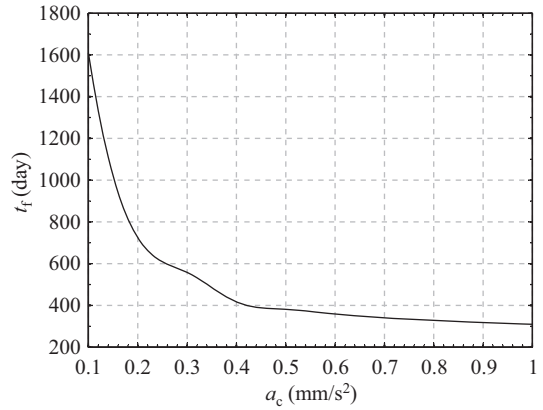

(c) Earth–Mars case

Fig. 7 Optimal three-dimensional orbit-to-orbit flight time t_f as a function of the characteristic acceleration a_c for an SFIDS-based spacecraft.

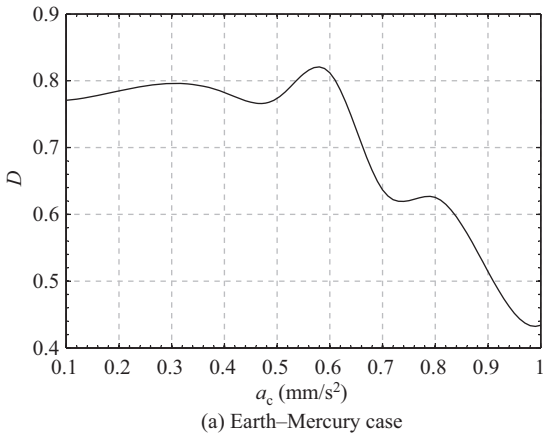

(a) Earth–Mercury case

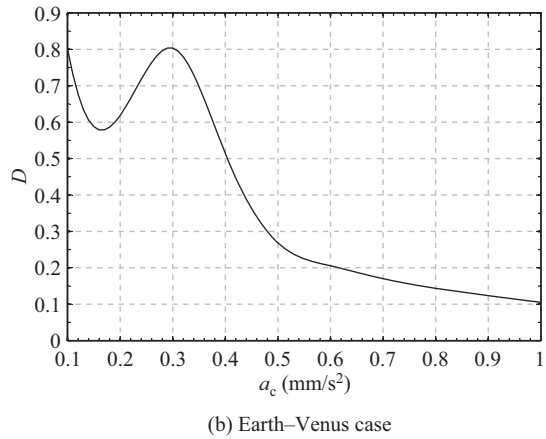

(b) Earth–Venus case

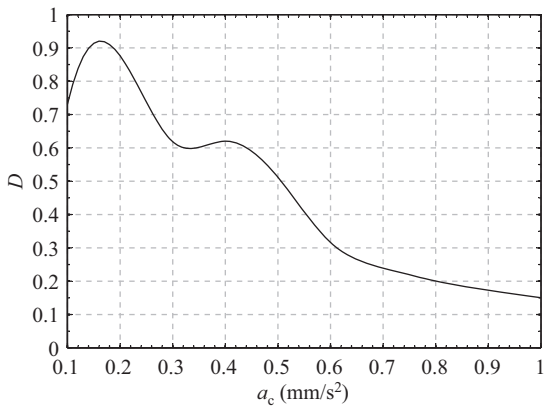

(c) Earth–Mars case

Fig. 8 Function $D = D(a_c)$ for the three mission cases; see Eq. (41).

exploration mission to the asteroid using a solar electric-powered spacecraft with the expected launch date in late September 2022. NASA's reference study on the Psyche mission included a solar electric cruise of approximately 3.5 years (with an estimated arrival in 2026), an intermediate Mars gravity assist, and a scientific observation period of 21 months around the target asteroid. Unfortunately, the launch was indefinitely postponed in June 2022.

The characteristics of the heliocentric orbit of the asteroid are listed in Table 1. These indicate that reaching this small body will be a challenge for a solar sail-based spacecraft because of the distance of the asteroid from the Sun. Indeed, the fact that the solar radiation pressure has an inverse-square variation with the solar distance

imposes severe constraints on solar sail-based transfers when the mean radius of the target orbit is larger than the mean Sun–Mars distance. Assuming a characteristic acceleration in the usual range $a_c \in [0.1, 1]$ mm/s^2, the minimum orbit-to-orbit flight time of the SFIDS-based spacecraft is shown in Fig. 9. The black circles refer to the cases listed in Table 2. The table also lists the optimal angular positions of the spacecraft (both at the beginning and end of the transfer) in terms of the true anomalies

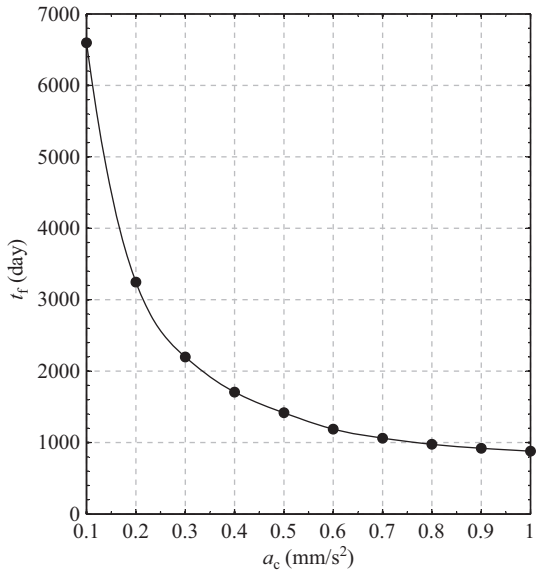

Fig. 9 Optimal flight time in a mission toward the asteroid 16 Psyche. Black circles refer to the scenarios detailed in Table 2.

Table 2 Optimal transfer trajectory characteristics in an Earth–16 Psyche orbit-to-orbit mission scenario

a_c (mm/s^2)	t_f (day)	$\nu(t_0)$ (deg)	$\nu(t_f)$ (deg)
1.0	880.1	92.2	105.5
0.9	919.8	78.9	109.8
0.8	975.9	54.6	112.1
0.7	1062.1	354.2	95.6
0.6	1188.0	280.8	64.0
0.5	1417.5	191.0	102.4
0.4	1706.5	149.2	145.1
0.3	2198.0	232.8	72.7
0.2	3245.5	207.2	109.8
0.1	6595.7	227.3	100.6

in the parking ($\nu(t_0)$) and target ($\nu(t_f)$) heliocentric orbits. The $\nu(t_0)$ and $\nu(t_f)$ values are the outputs of the optimization process. These provide the designer with useful information about the potential launch window at which the minimum transfer time can be achieved.

Figure 9 and Table 2 show that the SFIDS-based transfer toward the asteroid 16 Psyche with a flight time comparable to that of NASA's planned mission (i.e., approximately 3.5 years) requires a medium-performance sail with a characteristic acceleration in the range 0.5–0.6 mm/s^2. However, the SFIDS-based scenario considers a direct transfer, that is, it does not require an intermediate gravity-assisted maneuver. In this case, the diffractive solar sail option is less constrained from the viewpoint of the existing launch windows.

When a low-performance SFIDS is considered for mission optimization, the minimum flight time is in

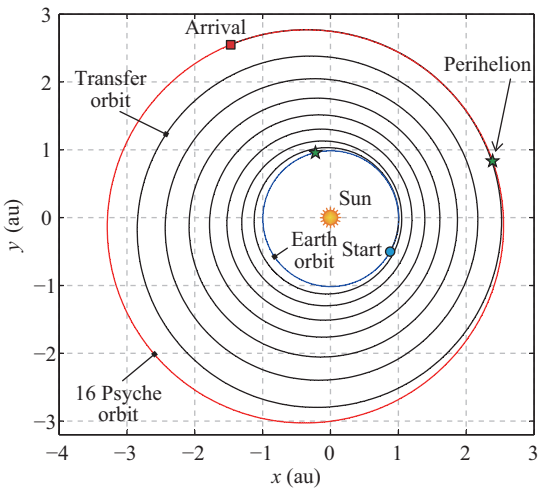

(a) Ecliptic projection

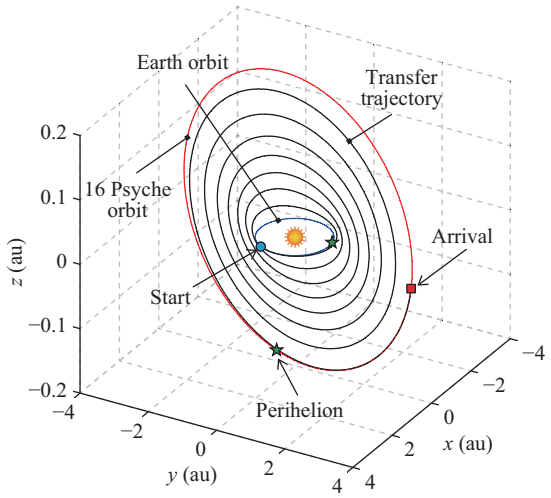

(b) Three-dimensional view (scale of z-axis is exaggerated)

Fig. 10 Optimal Earth–16 Psyche transfer trajectory of an SFIDS-based spacecraft with $a_c = 0.1$ mm/s^2.

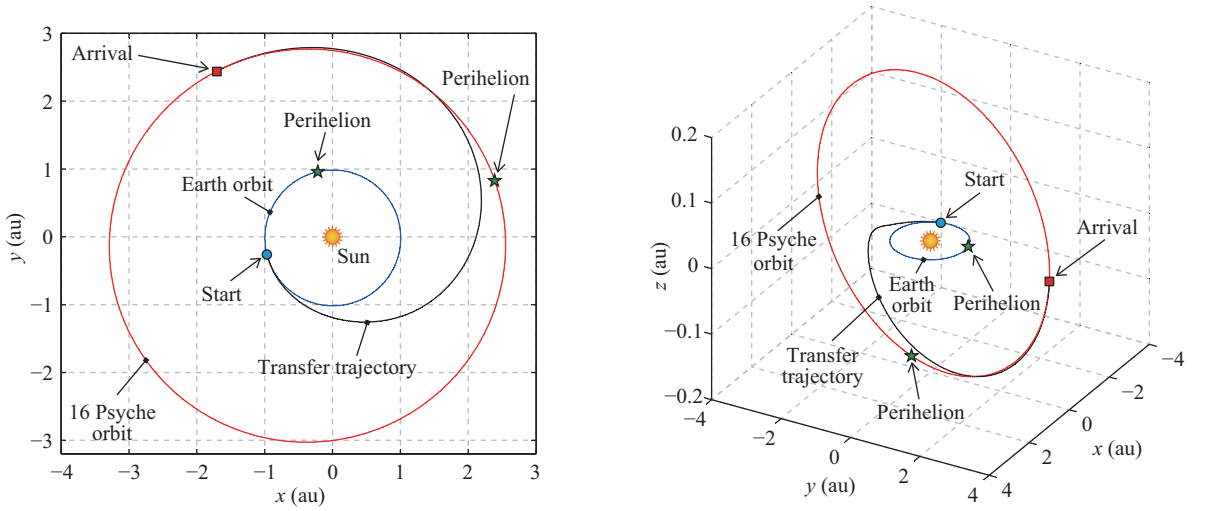

(a) Ecliptic projection (b) Three-dimensional view (scale of z-axis is exaggerated)

Fig. 11 Optimal Earth–16 Psyche transfer trajectory of an SFIDS-based spacecraft with $a_c = 1$ mm/s^2.

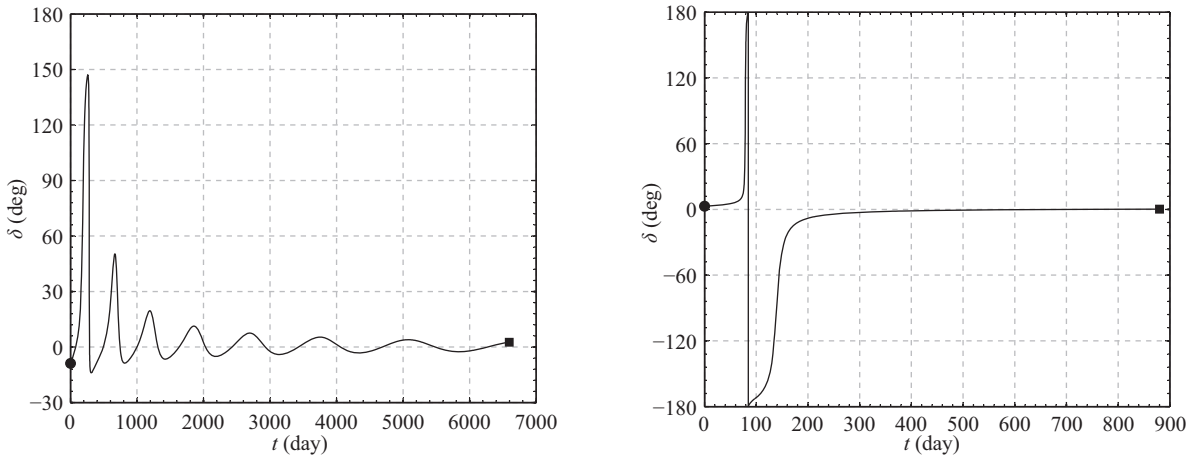

(a) Case of $a_c = 0.1$ mm/s^2 (b) Case of $a_c = 1$ mm/s^2

Fig. 12 Time variation of the optimal clock angle during the Earth–Psyche orbit transfer.

the order of 15–18 years, and the transfer trajectory shows multiple revolutions around the Sun. For example, Fig. 10 shows the optimal transfer trajectory when $a_c = 0.1$ mm/s^2, which requires approximately 18 years. However, using a medium-high performance sail in the mission design reduces the flight time to a few years and the complexity of transfer trajectory. For instance, Fig. 11 shows the optimal transfer trajectory when the characteristic acceleration is 1 mm/s^2. Figure 12 shows the time variation of the optimal clock angle during the transfer. It should be noted that in both low- and high-performance cases, the modulus of the clock angle remained below 20 deg for approximately 80% of the flight time. In the case of a high-performance sail, the $\nu(t_0)$ and $\nu(t_f)$ values listed in Table 2 indicate that the potential optimal launch window is around April 5, 2029.

6 Conclusions

This study analyzed the performance of a diffractive sail with a Sun-facing attitude in an optimal framework. Starting from the recent ideal thrust model of a diffractive sail and using an indirect approach, we derived the sail optimal control law, that is, the explicit expression of the clock angle (the single control variable of this

particular configuration) as a function of the osculating orbit-modified orbital elements and problem costates. The proposed mathematical model was then used to analyze the performance of an SFIDS as a function of the characteristic acceleration in a set of typical orbit-to-orbit interplanetary (three-dimensional) transfer scenarios.

The numerical simulations showed that for missions involving transfers toward both inner and outer planets, the flight times required by an SFIDS were significantly shorter than those required by a more conventional IRS, with the characteristic acceleration being the same. This is an interesting and less obvious result because the IRS has better maneuverability and may exploit the possible presence of coasting arcs along the transfer, which could be obtained by an edge-on flight orientation toward the Sun. The study of an orbit-to-orbit transfer toward the asteroid 16 Psyche also revealed that a medium-performance Sun-facing diffractive sail may achieve a flight time comparable to that of NASA's planned mission to Psyche.

The potential extensions of this study are twofold. First, the simplified thrust model discussed here can be used to analyze the SFIDS performance when generating and maintaining both artificial equilibrium points and heliocentric non-Keplerian orbits, paralleling the well-known results obtained with reflective solar sails. Second, the diffractive sail optimal performance can be analyzed by relaxing the Sun-facing attitude constraint, that is, by considering an additional control variable in the sail thrust model. In the latter case, the description of the sail propulsive acceleration vector becomes more complex (compared with the Sun-facing case), and requires a new study on the optimal control law.

Funding note

Open Access funding provided by Università di Pisa within the CRUI-CARE Agreement.

Declaration of competing interest

The authors have no competing interests to declare that are relevant to the content of this article.

References

[1] Fu, B., Sperber, E., Eke, F. Solar sail technology—A state of the art review. *Progress in Aerospace Sciences*, **2016**, 86: 1–19.

[2] Gong, S. P., MacDonald, M. Review on solar sail technology. *Astrodynamics*, **2019**, 3(2): 93–125.

[3] Bassetto, M., Quarta, A. A., Caruso, A., Mengali, G. Optimal heliocentric transfers of a Sun-facing heliogyro. *Aerospace Science and Technology*, **2021**, 119: 107094.

[4] Tsuda, Y., Mori, O., Funase, R., Sawada, H., Yamamoto, T., Saiki, T., Endo, T., Yonekura, K., Hoshino, H., Kawaguchi, J. Achievement of IKAROS—Japanese deep space solar sail demonstration mission. *Acta Astronautica*, **2013**, 82(2): 183–188.

[5] Tsuda, Y., Ono, G., Mimasu, Y. Classification of solar sail attitude dynamics with and without angular momentum. *Astrodynamics*, **2019**, 3(3): 207–216.

[6] Mori, O., Okuizumi, N., Chujo, T., Takao, Y. Improvement of sail storage and deployment mechanism for spin-type solar power sail. *Astrodynamics*, **2020**, 4(3): 223–231.

[7] Pezent, J., Sood, R., Heaton, A. High-fidelity contingency trajectory design and analysis for NASA's near-earth asteroid (NEA) Scout solar sail mission. *Acta Astronautica*, **2019**, 159: 385–396.

[8] Pezent, J. B., Sood, R., Heaton, A., Miller, K., Johnson, L. Preliminary trajectory design for NASA's Solar Cruiser: A technology demonstration mission. *Acta Astronautica*, **2021**, 183: 134–140.

[9] McInnes, C. R. *Solar Sailing: Technology, Dynamics and Mission Applications*. London: Springer, **1999**: 13–14, 46–54.

[10] Zola, D., Circi, C., Vulpetti, G., Scaglione, S. Photon momentum change of quasi-smooth solar sails. *Journal of the Optical Society of America A*, **2018**, 35(8): 1261–1271.

[11] Pino, T., Circi, C., Vulpetti, G. Wrinkling analysis for small solar-photon sails: An experimental and analytic approach for trajectory design. *Advances in Space Research*, **2019**, 63(11): 3675–3690.

[12] Davoyan, A. R., Munday, J. N., Tabiryan, N., Swartzlander, G. A., Johnson, L. Photonic materials for interstellar solar sailing. *Optica*, **2021**, 8(5): 722–734.

[13] Firuzi, S., Gong, S. P. Refractive sail and its applications in solar sailing. *Aerospace Science and Technology*, **2018**, 77: 362–372.

[14] Firuzi, S., Song, Y., Gong, S. P. Gradient-index solar sail and its optimal orbital control. *Aerospace Science and Technology*, **2021**, 119: 107103.

[15] Aspnes, E., Milster, T. D., Visscher, K. Optical force model based on sequential ray tracing. *Applied Optics*, **2009**, 48(9): 1642–1650.

[16] Bassetto, M., Caruso, A., Quarta, A. A., Mengali, G. Optimal steering law of refractive sail. *Advances in Space Research*, **2021**, 67(9): 2855–2864.

[17] Ashkin, A. Forces of a single-beam gradient laser trap on a dielectric sphere in the ray optics regime. *Biophysical Journal*, **1992**, 61(2): 569–582.

[18] Swartzlander, G. A. Radiation pressure on a diffractive sailcraft. *Journal of the Optical Society of America B*, **2017**, 34(6): C25–C30.

[19] Swartzlander, G. A. Flying on a rainbow: A solar-driven diffractive sailcraft. *Journal of the British Interplanetary Society*, **2018**, 71(4): 130–132.

[20] Srivastava, P. R., Swartzlander, G. A. Optomechanics of a stable diffractive axicon light sail. *The European Physical Journal Plus*, **2020**, 135(7): 570.

[21] Serak, S. V., Roberts, D. E., Hwang, J. Y., Nersisyan, S. R., Tabiryan, N. V., Bunning, T. J., Steeves, D. M., Kimball, B. R. Diffractive waveplate arrays. *Journal of the Optical Society of America B*, **2017**, 34(5): B56–B63.

[22] Srivastava, P. R., Chu, Y.-J. L., Swartzlander, G. A. Stable diffractive beam rider. *Optics Letters*, **2019**, 44(12): 3082–3085.

[23] Chu, Y., Firuzi, S., Gong, S. P. Controllable liquid crystal diffractive sail and its potential applications. *Acta Astronautica*, **2021**, 182: 37–45.

[24] Chu, Y.-J. L., Meem, M., Srivastava, P. R., Menon, R., Swartzlander, G. A. Parametric control of a diffractive axicon beam rider. *Optics Letters*, **2021**, 46(20): 5141–5144.

[25] Dubill, A. L., Swartzlander, G. A. Circumnavigating the Sun with diffractive solar sails. *Acta Astronautica*, **2021**, 187: 190–195.

[26] Quarta, A. A., Mengali, G., Niccolai, L. Smart dust option for geomagnetic tail exploration. *Astrodynamics*, **2019**, 3(3): 217–230.

[27] Quarta, A. A., Mengali, G., Denti, E. Optimal in-orbit repositioning of Sun-pointing smart dust. *Acta Astronautica*, **2019**, 154: 278–285.

[28] Niccolai, L., Bassetto, M., Quarta, A. A., Mengali, G. A review of Smart Dust architecture, dynamics, and mission applications. *Progress in Aerospace Sciences*, **2019**, 106: 1–14.

[29] Vulpetti, G., Circi, C., Pino, T. Coronal Mass Ejection early-warning mission by solar-photon sailcraft. *Acta Astronautica*, **2017**, 140: 113–125.

[30] Bassetto, M., Niccolai, L., Boni, L., Mengali, G., Quarta, A. A., Circi, C., Pizzurro, S., Pizzarelli, M., Pellegrini, R. C., Cavallini, E. Sliding mode control for attitude maneuvers of Helianthus solar sail. *Acta Astronautica*, **2022**, 198: 100–110.

[31] Caruso, A., Quarta, A. A., Mengali, G. Comparison between direct and indirect approach to solar sail circle-to-circle orbit raising optimization. *Astrodynamics*, **2019**, 3(3): 273–284.

[32] Quarta, A. A., Mengali, G., Bassetto, M. Optimal solar sail transfers to circular Earth-synchronous displaced orbits. *Astrodynamics*, **2020**, 4(3): 193–204.

[33] Heiligers, J., Fernandez, J. M., Stohlman, O. R., Wilkie, W. K. Trajectory design for a solar-sail mission to asteroid 2016 HO_3. *Astrodynamics*, **2019**, 3(3): 231–246.

[34] Tsuda, Y., Takeuchi, H., Ogawa, N., Ono, G., Kikuchi, S., Oki, Y., Ishiguro, M., Kuroda, D., Urakawa, S., Okumura, S. I., *et al.* Rendezvous to asteroid with highly uncertain ephemeris: Hayabusa2's Ryugu-approach operation result. *Astrodynamics*, **2020**, 4(2): 137–147.

[35] Mori, O., Matsumoto, J., Chujo, T., Matsushita, M., Kato, H., Saiki, T., Tsuda, Y., Kawaguchi, J., Terui, F., Mimasu, Y., *et al.* Solar power sail mission of OKEANOS. *Astrodynamics*, **2020**, 4(3): 233–248.

[36] Walker, M. J. H., Ireland, B., Owens, J. A set modified equinoctial orbit elements. *Celestial Mechanics*, **1985**, 36(4): 409–419.

[37] Walker, M. J. H. A set of modified equinoctial orbit elements. *Celestial Mechanics*, **1986**, 38(4): 391–392.

[38] Betts, J. T. Very low-thrust trajectory optimization using a direct SQP method. *Journal of Computational and Applied Mathematics*, **2000**, 120(1–2): 27–40.

[39] Wright, J. L. *Space Sailing*. Taylor & Francis, **1992**: 223–233.

[40] Bassetto, M., Quarta, A. A., Mengali, G., Cipolla, V. Trajectory analysis of a Sun-facing solar sail with optical degradation. *Journal of Guidance, Control, and Dynamics*, **2020**, 43(9): 1727–1732.

[41] Bassetto, M., Quarta, A. A., Mengali, G., Cipolla, V. Spiral trajectories induced by radial thrust with applications to generalized sails. *Astrodynamics*, **2021**, 5(2): 121–137.

[42] Mengali, G., Quarta, A. A. Optimal control laws for axially symmetric solar sails. *Journal of Spacecraft and Rockets*, **2005**, 42(6): 1130–1133.

[43] McInnes, C. R. Passive control of displaced solar sail orbits. *Journal of Guidance, Control, and Dynamics*, **1998**, 21(6): 975–982.

[44] Pathak, S. Photonics integrated circuits. In: *Nanoelectronics*. Amsterdam: Elsevier, **2019**: 219–270.

[45] Dachwald, B., Mengali, G., Quarta, A. A., MacDonald, M. Parametric model and optimal control of solar sails with optical degradation. *Journal of Guidance, Control, and Dynamics*, **2006**, 29(5): 1170–1178.

[46] Vulpetti, G., Apponi, D., Zeng, X. Y., Circi, C. Wrinkling analysis of solar-photon sails. *Advances in Space Research*, **2021**, 67(9): 2669–2687.

[47] Bianchi, C., Niccolai, L., Mengali, G., Quarta, A. A. Collinear artificial equilibrium point maintenance with a

wrinkled solar sail. *Aerospace Science and Technology*, **2021**, 119: 107150.

[48] Mengali, G., Quarta, A. A. Optimal three-dimensional interplanetary rendezvous using non-ideal solar sail. *Journal of Guidance, Control, and Dynamics*, **2005**, 28(1): 173–177.

[49] Caruso, A., Niccolai, L., Quarta, A. A., Mengali, G. Effects of attitude constraints on solar sail optimal interplanetary trajectories. *Acta Astronautica*, **2020**, 177: 39–47.

[50] Mengali, G., Quarta, A. A. Rapid solar sail rendezvous missions to asteroid 99942 Apophis. *Journal of Spacecraft and Rockets*, **2009**, 46(1): 134–140.

[51] Stengel, R. F. *Optimal Control and Estimation*. Dover Publications, **1994**: 222–254.

[52] Betts, J. T. Survey of numerical methods for trajectory optimization. *Journal of Guidance, Control, and Dynamics*, **1998**, 21(2): 193–207.

[53] Bryson, A. E., Ho, Y. C. *Applied Optimal Control*. New York: Hemisphere Publishing Corporation, **1975**: 71–89.

[54] Shampine, L. F., Reichelt, M. W. The MATLAB ODE suite. *SIAM Journal on Scientific Computing*, **1997**, 18(1): 1–22.

[55] Palmeri, F., Tortorici, D., Laurenzi, S., Circi, C., Santonicola, M. G., Pizzarelli, M., Pizzurro, S., Pellegrini, R., Cavallini, E. Structural design of booms for the solar sail of helianthus sailcraft. In: Proceedings of the 73rd International Astronautical Congress, Paris, France, **2022**.

[56] Quarta, A. A., Mengali, G. Semi-analytical method for the analysis of solar sail heliocentric orbit raising. *Journal of Guidance, Control, and Dynamics*, **2012**, 35(1): 330–335.

[57] Sirohi, R., Moore, R. R., Deforrest, L. R., Thornton, M. S., Larson, K. L., Wenkert, D. D., Kazz, G. J. Psyche mission's end-to-end information system architecture: Advantages, challenges, and operability. In: *Space Operations*. Cham: Springer, **2022**: 107–139.

[58] Elkins-Tanton, L., Asphaug, E., Bell, J., Bierson, C., Bills, B., Bottke, W., Courville, S., Dibb, S., Jun, I., Lawrence, D., *et al.* Distinguishing the origin of asteroid (16) Psyche. *Space Science Reviews*, **2022**, 218(3): 17.

[59] Jaumann, R., Bell, J., Polanskey, C., Raymond, C., Aspaugh, E., Bercovici, D., Bills, B., Binzel, R., Bottke, W., Christoph, J., *et al.* The psyche topography and geomorphology investigation. *Space Science Reviews*, **2022**, 218(2): 7.

[60] Collinson, G. A., Chen, L. J., Jian, L. K., Dorelli, J. The solar wind at (16) Psyche: Predictions for a metal world. *The Astrophysical Journal Letters*, **2022**, 927(2): 202.

Alessandro A. Quarta received his Ph.D. degree in aerospace engineering from the University of Pisa, Italy, in 2005 and, currently, he is a professor of flight mechanics at the Department of Civil and Industrial Engineering of the University of Pisa. His main research areas include spaceflight simulation, spacecraft mission analysis and design, low-thrust trajectory optimization, solar sail, and E-sail dynamics and control. E-mail: a.quarta@ing.unipi.it

Giovanni Mengali received his Doctor of Engineer degree in aeronautical engineering in 1989 from the University of Pisa, Italy. Since 1990, he has been with the Department of Aerospace Engineering (now Department of Civil and Industrial Engineering) of the University of Pisa, first as a Ph.D. student, then as an assistant and an associate professor. Currently, he is a professor of space flight mechanics. His main research areas include spacecraft mission analysis, trajectory optimization, solar sails, electric sails, and aircraft flight dynamics and control. E-mail: g.mengali@ing.unipi.it

Marco Bassetto received his Ph.D. degree in civil and industrial engineering at the Department of Civil and Industrial Engineering of the University of Pisa, Italy. From January 2020 to June 2021, he was the holder of a scholarship entitled "Dynamic analysis and control of an E-Sail" at the same department, where he also was a research assistant from July 2021 to June 2022, and he is currently an assistant professor of aerospace systems. His research activity focuses on trajectory design and attitude control of spacecraft propelled with low-thrust propulsion systems such as solar sails and electric solar wind sails. E-mail: marco.bassetto@ing.unipi.it

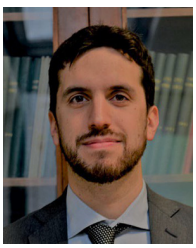

Lorenzo Niccolai received his Ph.D. degree in industrial engineering (aerospace curriculum) from the University of Pisa, Italy, in 2018. He was a research assistant at the Department of Civil and Industrial Engineering of the University of Pisa from 2019 to 2020. He is currently an assistant professor of spaceflight mechanics at the same department. His research interests include mission design, low-thrust trajectory analysis and control, with special attention on innovative propulsive concepts such as solar sails and electric solar wind sails. E-mail: lorenzo.niccolai@unipi.it